

pubs.acs.org/journal/apchd5 Letter

Optical-Pump Terahertz-Probe Spectroscopy of the Topological Crystalline Insulator $Pb_{1-x}Sn_xSe$ through the Topological Phase Transition

Zhenyang Xiao,* Jiashu Wang, Xinyu Liu, Badih A. Assaf, and David Burghoff



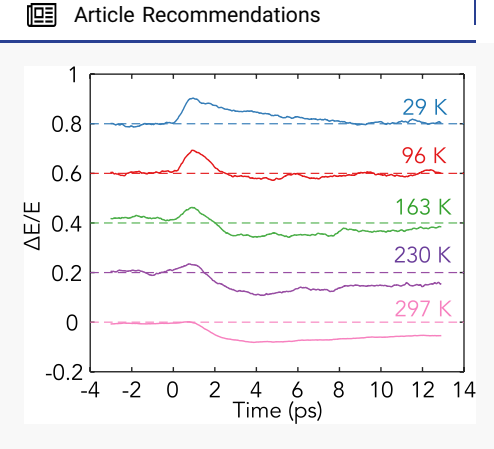
Cite This: ACS Photonics 2022, 9, 765-771



ACCESS

III Metrics & More

ABSTRACT: Topological crystalline insulators, topological insulators whose properties are guaranteed by crystalline symmetry, can potentially provide a promising platform for terahertz optoelectronic devices, as their properties can be tuned on demand when layered in heterostructures. We perform the first optical-pump terahertz-probe spectroscopy of topological crystalline insulators, using them to study the dynamics of $Pb_{1-x}Sn_xSe$ as a function of temperature. At low temperatures, excitation of Dirac fermions leads to an increase in terahertz transmission; from this negative photoconductivity, the intrasubband relaxation rate of 6 ps is extracted. At high temperatures, where only massive Fermions exist, the free-carrier losses induced by the pump reduce the terahertz transmission for the duration of the 27 ps interband lifetime. Both effects are present at temperatures near the topological-to-trivial transition. Our experimental observations provide critical details for potential applications of $Pb_{1-x}Sn_xSe$ and provide a direct measurement of the topological character of $Pb_{1-x}Sn_xSe$ heterostructures.



KEYWORDS: topological crystalline insulators, dynamics, optical-pump terahertz-probe spectroscopy, conductivity, Dirac fermions

Recent progress in topological insulators (TIs) has pointed to them as promising platforms for terahertz and farinfrared heterostructure devices. 1-3 TIs are novel materials with insulating bulk bandgaps and gapless surface states, which are promising platforms for devices with novel functionalities. 4-6 TI material can potentially be protected against defects and can have tunable inverted bandgaps. There are two kinds of TI materials, the canonical topological materials and the topological crystalline insulators (TCI). The canonical topological materials are narrow-gap semiconductors with an inverted band structure, such as bismuth or antimony chalcogenides.7 As for TCIs, they possess a crystalline symmetry that guarantees the existence of an even number of surface states.8 As one of the well-known TCI materials, lead-tin-selenide ($Pb_{1-x}Sn_xSe$) has recently been reported as an interesting candidate for terahertz optoelectronic heterostructures, as its properties can be tuned using either the Sn concentration or the temperature.³ In addition, certain alloy fractions remain inverted even at room temperature. In principle, this could lead toward the creation of engineered topological states, whose wave functions are designed to achieve a particular optical or electrical response. For example, one can imagine terahertz sources⁹⁻¹¹ or detectors^{12,13} that operate at higher temperatures by relying on states that are protected from scattering by their topological nature, not by a reduction in overlap. However, there is still a long way to go

toward making optoelectronic devices out of these novel materials. Understanding the carrier dynamics and photoconductivity is the first obstacle for creating optoelectronic devices.

Optical-pump terahertz-probe spectroscopy (OPTP) and time-resolved angle-resolved photoemission spectroscopy (tr-ARPES) are common methods used in the TI dynamical studies. Tr-ARPES is a powerful tool for studying nonequilibrium quantum states, as it enables imaging of electron dynamics of an optically excited state directly in momentum space. However, the bulk band structure of TIs measured in this method is largely masked by the topological surface states. In contrast, terahertz time-domain spectroscopy (THz-TDS) and ultrafast optical-pump terahertz-probe spectroscopy (OPTP) can directly interrogate the dynamics of free carriers by manipulating the photoinduced transmittance. Since light penetrates into the TI material, both bulk and surface carriers' information can be obtained. They

Received: November 8, 2021 Published: March 4, 2022





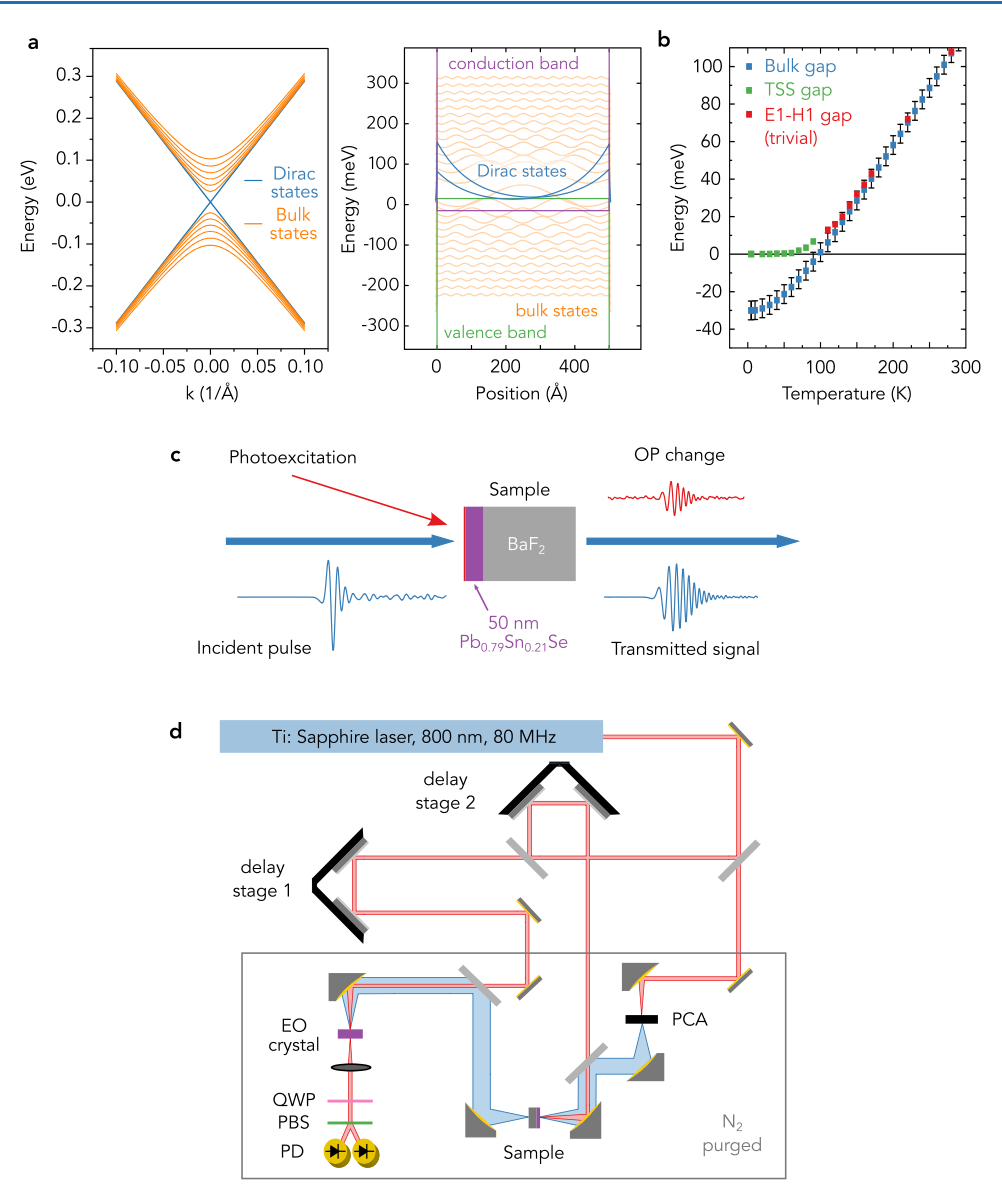


Figure 1. System and $Pb_{1-x}Sn_xSe$ (x=0.21) sample information. (a) Calculated band diagram of the $Pb_{1-x}Sn_xSe$ (x=0.21) film at 4.2 K (left), and zone center ($k_t=0$) wave functions (right). (b) Gap information on $Pb_{1-x}Sn_xSe$ (x=0.21) vs temperature. The bulk bandgap is represented by the blue squares, the bandgaps of the topological surface states (TSSs) are represented by green squares, and the red squares represent the E1 gap (the gap of the lowest subband when trivial). (c) Simplified version of the optical-pump terahertz-probe spectroscopy (OPTP) measurement. (d) Detailed schematic of OPTP system setup.

are particularly useful for investigations of Dirac materials, as has been demonstrated in studies of the photoinduced carrier dynamics in graphene and Bi₂Se₃. OPTP systems can provide a time-resolved measurement for studying the photoexcited carriers generated by ultrafast infrared pulses, allowing the carrier dynamics related to the photoexcitation and photorelaxation to both be extracted. As an important 2D material, graphene has been extensively studied by OPTP measurements, and anomalous negative photoinduced conductivity has been found. This negative photoconductivity was first observed in graphene monolayers produced by chemical vapor deposition (CVD) methods, and it was subsequently observed in Bi₂Se₃ thin films as well.

In this work, we study the carrier dynamics of the TCI $Pb_{1-x}Sn_xSe$ as a function of temperature using optical-pump terahertz-probe spectroscopy. At low temperatures (T = 29 K), we observe negative photoconductivity introduced by the

photoexcitation, similar to what has been observed in Bi_2Se_3 and graphene. A decay time of about 6 ps is observed for the hot Dirac electrons causing the negative conductivity. Both positive and negative photoconductivity are observed at different pump delay positions at moderate temperatures (T=96,163, and 230 K), which can be explained by the coexistence of the Dirac fermions from the gapless surface states and the massive Fermions from the bulk states. At room temperature (T=297 K), only massive Fermions are present, as the gapless Dirac cone is gapped, and the induced photoconductivity decays at a rate of about 27 ps. These observations provide critical details for potential applications of $Pb_{1-x}Sn_xSe$ and provide a direct measurement of the topological character of topological surface states.

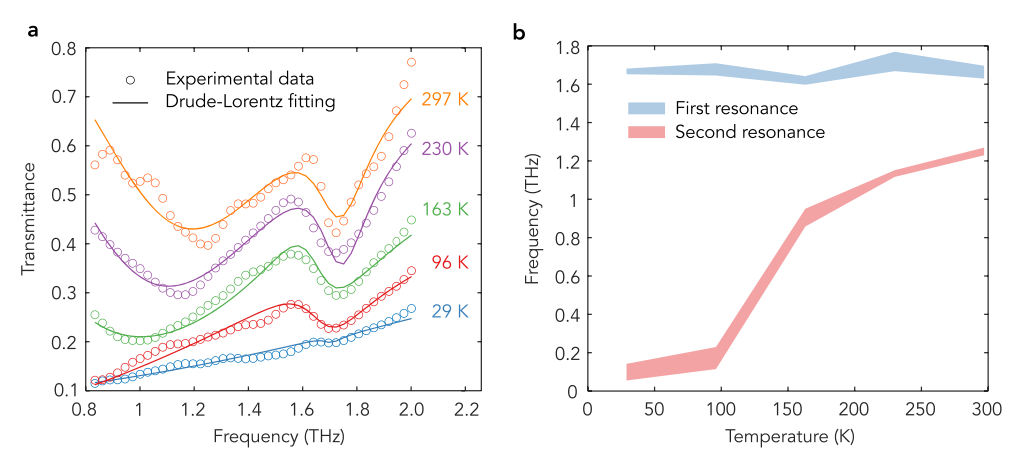


Figure 2. (a) $Pb_{1-x}Sn_xSe$ (x = 0.21) transmittance at different temperatures. Measurements are indicated by circles and the Drude-Lorentz fittings are indicated by lines. (b) Resonance frequencies as a function of temperature. The widths of the curves represent one standard deviation.

RESULTS AND DISCUSSION

For this work, we grew a 50 nm quantum well of $Pb_{1-x}Sn_xSe$ of BaF_2 (111) with a 5 nm EuSe capping layer to protect from oxidation. $Pb_{1-x}Sn_xSe$ is a well-known TCI material that can exhibit a topological transition from a trivial insulator to TCI under modification of chemical composition, temperature, or pressure, while EuSe is topologically trivial. The layers are grown following the procedure described in ref 27, directly on the BaF_2 surface, without the buffer layer stack. The band structure parameters of bulk $Pb_{1-x}Sn_xSe$ has been investigated at different Sn compositions and temperatures, with a band gap E_g that can be approximately expressed by Pa_g

$$E_{\rm g}(x, T) = E_{\rm g}(x, 4.2) + 2(\sqrt{22.5^2 + (0.32 \text{ K}^{-1})^2 (T - 4.2 \text{ K})^2} - 22.5)$$

(meV)

$$E_{\rm g}(x, 4.2) = 2(72 - 710x + 2440x^2 - 4750x^3) \text{ (meV)}$$
(1)

where x is the composition fraction of the Sn, T is the temperature, and $E_{\rm g}(x,~4.2)$ is the energy gap at 4.2 K. Equation 1 is most accurate when 0 < x < 0.3 and $4.2~{\rm K} < T < 200~{\rm K}$. The Sn content of the films can deduced from X-ray diffraction measurements using Vegard's law as done in ref 28. We find $x = 0.21 \pm 0.1$. We approximate the value of the energy gap at 4.2 K to be $E_{\rm g} = -30 \pm 5~{\rm meV}$ from eq 1. Hall measurements indicate that the samples are p-doped at low temperature with an estimated hole concentration of $7.8 \times 10^{18}~{\rm cm}^{-3}$.

The band structure of the 50 nm $Pb_{1-x}Sn_xSe$ (x=0.21) can now be calculated using an envelope function method, ²⁹ previously used in refs 27 and 28. Following the basis and model shown in ref 27, the k.p. matrix Hamiltonian of $Pb_{1-x}Sn_xSe$, is utilized for this operation, with $k_z=-i\partial_z$. The energy gap of the TCI well is fixed at $E_g=-30$ meV at low temperature. The energy gap in the barrier is fixed to 2 eV. Both the substrate and the capping layer have a wide energy gap exceeding 1 eV, however, we have checked that varying energy gap of the barriers in the model above 1 eV has a minimal impact on the band structure of the Dirac states of the material. The band offsets of the conduction and the valence bands are assumed equal and opposite in sign to account for the band inversion that takes place at the interface.

We fix the k.p. matrix along the growth direction to $\hbar \nu_z = 2.6 \text{ eV} \cdot \text{Å}$ and we assume the bulk valleys to be isotropic so that $\nu_z = \nu_{xz}$ as typically seen for $\text{Pb}_{1-x} \text{Sn}_x \text{Se}$ with x > 0.20. The

model yields the band dispersion shown in Figure 1a, with gapless Dirac surface states dispersing the energy gap formed by the quantum well subbands. To model the temperature dependence of the band structure, we use the energy dependent gap empirically determined from eq 1, a repeat of our calculations with $E_{\rm g}(0.21,\,T)$ implemented in the model for various T. The model yields the energy gap of the topological surface states (TSS) in the topological regime as it evolves from 0 meV up to a few meV when $E_{\rm g}(0.21,\,T)$ is small but negative. When $E_{\rm g}(0.21,\,T)$ becomes positive, the model is equivalent to that of a conventional narrow gap semiconductor and yields the energy separation between the topmost hole subband H1 and bottom most electron subband E1. The evolution of the TSS gap and that of E1–H1 gap is shown in Figure 1b.

As can be seen in Figure 1b, a topological phase transition is seen to happen at 110 ± 15 K (the uncertainty is due to the propagated uncertainty of E_g). When the temperature goes lower than this point, the topological surface states (TSS) with a gapless Dirac point appears, and the carrier in those states become so-called Dirac Fermions. With our knowledge of the bulk gap, we can compute the band dispersion of the Dirac states and its gap acquisition through transition. The unique massless Dirac fermions in the surface states are the key to understand the dynamics present in this material. In order to study those dynamics, OPTP is used. The principle of this system can be seen in Figure 1c: a high-power short-pulse laser is used to excite both a photoconductive antenna (PCA) and the sample, and the terahertz generated by the PCA is passed through the sample and modified by the photoexcited carriers. The terahertz signal is then detected using electro-optic sampling in a ZnSe crystal and balanced detection. The detailed OPTP system setup is shown in Figure 1d. The pulsed laser used in our OPTP system was at 800 nm (1.55 eV) with a duration of 86 fs and a repetition rate of 80 MHz. It is split into three beams: one to excite the PCA for terahertz generation, one to work as a probe for scanning the terahertz signal, and one to excite the sample. A dual lock-in amplifier scheme is used to remove long-term drift, with the PCA and excitation pump being modulated at 10 kHz and 220 Hz, respectively. Two lock-in amplifiers are used to measure the transmitted terahertz. One represents the difference in terahertz with the pump on versus the pump off (for measuring the changes induced by sample excitation), while the other represents the average (for the reconstruction of the TDS signal). These two

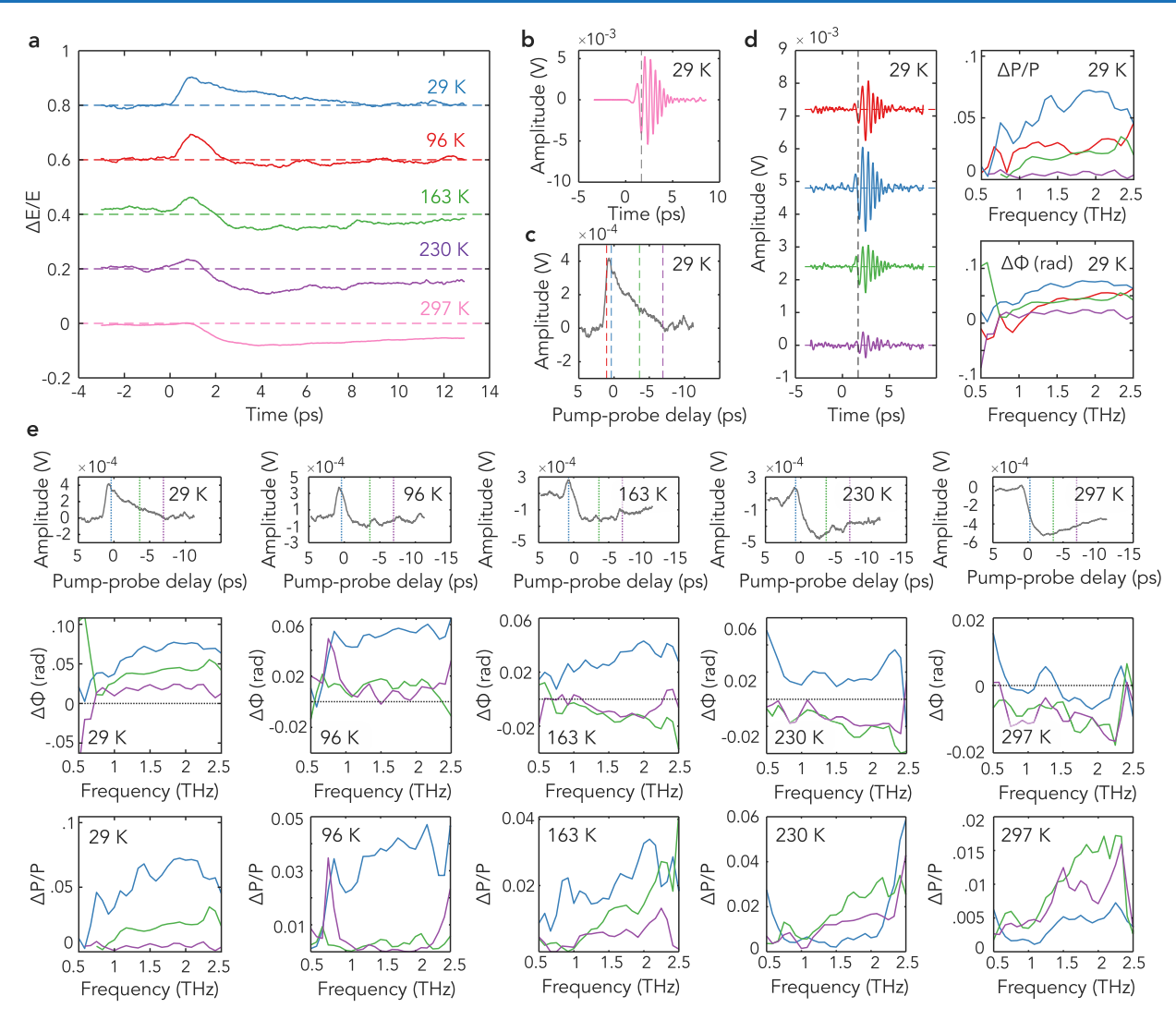


Figure 3. (a) Effect of an optical pump on the amplitude of the transmitted terahertz pulse at different temperatures, offset for clarity. (The dashed lines indicate the offset for each curve.) An increase in the transmission is notable at low temperatures, while only a decrease is evident at high temperatures. (b) Transmitted TDS pulse shape of $Pb_{1-x}Sn_xSe$ at 29 K. (c) OP pulse-induced difference of THz field through $Pb_{1-x}Sn_xSe$ at 29 K as a function of pump–probe delay. (d) Dual lock-in difference signal measured at different pump delays marked in (c), in both time (left) and frequency (right) domain. (e) Temperature dependence of transient scans. The upper figure shows the OP-induced difference of the THz field through $Pb_{1-x}Sn_xSe$ as a function of the pump–probe delay at 29, 96, 163, 230, and 297 K, respectively, the middle figure shows the photoinduced phase at the pump delays marked in the upper figure, and the lower figure shows the photoinduced changes in amplitude at different pump delays marked in the upper figure.

signals are combined to produce the spectrum with the pump on and with the pump off. Due to the limitation of the high repetition rate of our Ti:sapphire laser, the optical pump beam's fluence at the sample was limited to $1.6~\mu\text{J/cm}^2$ for all measurements. The bandwidth of our system is about 6 THz, and the SNR is about 60 dB.

Using the time-domain system, we first measured the transmittance of the $Pb_{1-x}Sn_xSe$ (x=0.21) sample as the temperature is changed. As shown in Figure 2a, we focus on five temperature points, two of which (29 and 96 K) are well below the temperature point at which there exist topological surface states, and three that are above (163, 230, and 297 K). The transmittance is calculated by comparing the signal through a substrate without the TCI to one that is measured with the TCI. Due to the lower SNR at the two sides of the spectrum, we select only the highest SNR region from 0.7 THz to 2 THz for analysis, below the Reststrahlen band of the BaF₂ substrate, and fit the transmittance data using a Drude—

Lorentz model. Due to the observation that two valleys are present in the transmittance spectrum from 163 to 297 K, we applied two resonance terms in the Drude-Lorentz model to extract detailed information about those resonances. The resonance frequencies extracted by the Drude-Lorentz model are shown in Figure 2b as a function of temperature. By adding white noise to the experimental data and iteratively repeating the Drude-Lorentz fitting, the standard deviation is calculated as well. Two pronounced resonances are observed: one at 1.7 THz (7 meV) that is relatively constant in temperature, and one lower-frequency branch that is strongly temperaturedependent, below 1.2 THz (5 meV). Neither can be attributed to direct electronic transitions, as the energies are too low to be explained by intersubband absorption ($\Delta E > 14$ meV for all occupied subbands). We attribute the constant-temperature resonance as arising from weak coupling to bulk TO phonons, as this frequency occurs close to the value previously measured by FTIR spectroscopy (50 cm⁻¹).³⁰ The strongly temperature-

dependent resonance can perhaps be best explained as coupling to shear vertical surface modes, which were previously found (in Pb_{0.7}Sn_{0.3}Se) to have energies that strongly depend on the emergence of Dirac fermions, shifting to low energies at temperatures below the transition.³¹ This effect arises as a result of the strong electron—phonon interaction but requires further study.

After the transmittance spectra of the $Pb_{1-x}Sn_xSe$ sample were obtained using normal time-domain spectroscopy, OPTP measurements were performed. By locating the first stage of the TDS signal at the point marked by the black dashed line in Figure 3b and scanning the delay of the high-power infrared pump pulse, information about the time-resolved carrier dynamics could be measured, as is shown in Figure 3a. Figure 3b-d shows an example of the time scale of the detailed OP signal at 29 K. (Note that the delay time axis numbers are different for the same curve in Figure 3a,c, since we are using different times as the time reference point. Figure 3a uses the time when the pump laser arrived on the sample as the reference point, while Figure 3c uses the time when the terahertz signal arrives on the EO crystal as the reference point to show a clearer relation between the TDS signal and OP signal in the time domain.) All pump delays shown here aside from Figure 3a are using the second time axis. As shown in Figure 3b, as the probe delay is fixed at 1.67 ps, marked by the black dashed line, we scanned the pump delay to monitor timeresolved carrier dynamics at 29 K. In Figure 3c, one can see that the transmitted field reaches a maximum at a pumpprobe delay of 0.7 ps (with a 1 ps rise time) and then decays over the next 6 ps. In order to investigate the frequency response, the change in the transmitted signal induced by the pump was plotted at several pump-probe delays. Each curve in Figure 3d represents the transmitted pulse at the different time points marked with the same color dash line in Figure 3c. These are also converted into the frequency domain. Note that the optical pump does not induce a strong frequency dependence in the transmission, as is expected of the optical properties of Dirac cones. (Because the transmission and fluence of the system is limited, the frequency-dependent spectra all have limited signal-to-noise ratio. Some caution must be exercised when interpreting any narrowband features that appear to be present.)

Figure 3a illustrates the photoexcited carrier dynamics as a function of temperature. At room temperature (T = 297 K), the transmittance of the sample decreases as the pump pulse arrives at the sample. This is a well-explained phenomenon that is justified by increase of the number of free carriers. At this temperature point, the sample has a bandgap around 115 meV, which makes its behavior similar to conventional semiconductors: only massive Fermions are present, the gapless Dirac cone does not exist, and due to the increase of the free carrier concentration, the transmittance decreases after photoexcitation. The induced photoconductivity at room temperature decays at a rate of about 27 ps due to interband scattering. However, at low temperatures (T = 29 K), an increase in transmittance after the sample is excited is observed. This is an anomalous phenomenon that has also been observed in some well-explored 2D materials, such as Bi₂Se₃ and graphene. ^{20-23,25,32} A decay time of about 6 ps is observed. A combination of positive and negative photoconductivity is observed at different pump delay positions at moderate temperatures (T = 96, 163, and 230 K), which can be explained by the coexistence of the Dirac fermions from the

gapless surface states and the massive fermions from the bulk states. We also find that the strength of the pump-induced signal is also changing with temperature. As the temperature is lowered, the effect of the massive electrons is reduced, as the low fluence ensures that the incident light is screened by the Dirac fermions. This is also apparent in the phase of the difference field, shown in Figure 3e. Though the signal-to-noise ratio in the frequency domain is limited by the limited transmission through the sample and low excitation fluence, it is apparent that pump-probe delays corresponding to an increase in transmission are associated with a positive difference phase. This is particularly evident at 163 and 230 K shown in Figure 3e, which have both an increase and a decrease in transmission (depending on the pump-probe delay), which manifests as the phase-changing sign. Such an effect is expected from the induced photoconductivity changing sign. Note that the fluence is low and that all phase changes are under 0.1 radians, so the measurement of Figures 3a at a fixed delay essentially represents the integrated transmission change.

To further explore the anomalous transmittance increase at low temperatures, we calculate the photoconductivity of the sample at $29~\mathrm{K}$ using 33

$$T(\omega) = \frac{1+n}{(1+n+Z_0G(\omega))e^{i\phi}}$$
(2)

where $T(\omega)$ is the complex transmittance of the sample, n is the refractive index of the substrate, Z_0 is the impedance of free space, $G(\omega)$ is the conductivity, and ϕ is the phase difference introduced by the thickness difference of the substrate and the $Pb_{1-x}Sn_xSe$ sample.

Figure 4a shows the calculated real and imaginary parts of the conductivity as a function of frequency for the unpumped sample. The pumped sample is very similar, so in Figure 4b we

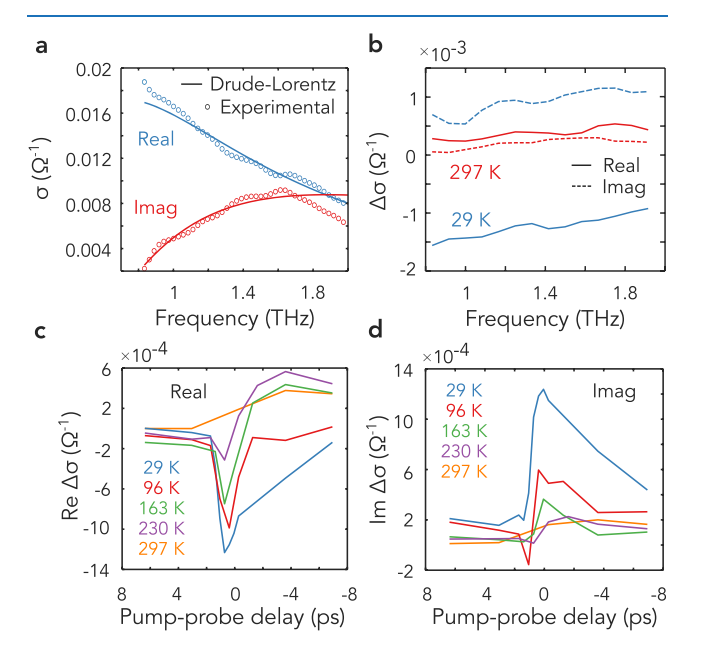


Figure 4. (a) Real and imaginary parts of the conductivity (σ) at 29 K with no optical pump. (b) Real and imaginary parts of the photoinduced conductivity $(\Delta\sigma)$ near the maximum $\Delta E/E$ position (0.39 ps pump delay at 29 K and -3.61 ps pump delay at 297 K). (c) Real part of the time-dependent photoinduced conductivity. (d) Imaginary part of the time-dependent photoinduced conductivity.

plot the differential conductivity. To better understand the physical origin of the photoinduced conductivity here, the conductivity is fitted with a two-term Drude–Lorentz model, including a Drude term, a Drude–Lorentz term (which modeling the TO phonon resonance), and a frequency-independent contribution to the dielectric constant (which accounts for the effect of higher-energy excitations):^{26,34}

$$G_{j}(\omega) = \left(-\frac{\omega_{\text{pD}}^{2}}{i\omega - \Gamma_{\text{D}}} - \frac{i\omega\omega_{\text{pDL}}^{2}}{\omega_{\text{DL}}^{2} - \omega^{2} - i\omega\Gamma_{\text{DL}}} - i(\epsilon_{\infty} - 1)\omega\right)\epsilon_{0}d\tag{3}$$

where $\omega_{\rm pD}$ is the plasma frequency of the Drude oscillator, $\Gamma_{\rm D}$ is the scattering rate of the Drude oscillator, ϵ_{∞} is the dielectric constant at high frequency, d is the sample thickness, and $\omega_{\rm pDL}$ and $\Gamma_{\rm D}$ are the parameters for the Lorentz oscillator.

The origin of the negative photoinduced conductivity can be understood by considering the Drude conductivity in the lowfrequency limit. The low-frequency conductivity dynamics are

governed by the Drude weight $D_{\rm Drude} = \frac{{\rm d}\omega_{\rm pD}^2}{(2\pi)^2}$ and the scattering rate $\Gamma_{\rm Drude}$, which is related to the carrier concentration and the mobility, respectively. The real part of the conductivity is determined by the ratio of the Drude weight and the scattering rate. For conventional semiconductors with bandgaps, the real part of photoinduced conductivity typically increases since the photoinduced carriers increase the Drude weight. For Dirac cones, this effect is typically offset by an increase in scattering rate, as the photoexcited electrons become hot. At room temperature, the ${\rm Pb}_{1-x}{\rm Sn}_x{\rm Se}$ sample possesses only massive states, which makes it behave like conventional semiconductors. However, as the temperature lowers, the surface states become gapless and the increase of scattering rate becomes dominant, leading to a negative photoinduced conductivity.

To confirm that the scattering rate increases, we fit the complex conductance spectra to the same Drude–Lorentz model with and without the pump. While the Drude weight $D_{\rm Drude}$ of the pumped ${\rm Pb}_{1-x}{\rm Sn}_x{\rm Se}$ (x=0.21) sample increased by 2.1%, consistent with a small increase in the density of free carriers, a much larger increase of the scattering rate, $\Delta\Gamma_{\rm D}=47.8\%$, is observed. As a result, the ratio $\frac{D_{\rm Drude}}{\Gamma_{\rm Drude}}$ actually decreases. This causes the real part of the photoinduced conductivity, $\delta G \equiv G_{\rm pumped} - G_{\rm unpumped}$, to be negative, as is shown in Figure 4b. This explains the anomalous increase of the signal after the photoexcitation. Therefore, the 6 ps decay rate of the negative photoconductivity should be interpreted as an intrasubband (i.e., intra-Dirac cone) relaxation rate, not as a lifetime of the Dirac fermions.

To further explore the photoinduced conductivity at different pump delays, we extracted the photoinduced conductivity at all measured pump delays, as shown in Figure 4c,d. Since the photoinduced conductivity obtained at all temperatures and pump delays did not have a strong frequency dependence, we averaged the photoinduced conductivity in the frequency domain to examine the time-dependence. As expected, the real part of the photoinduced conductivity is negative when the Dirac fermions exist after excitation and decreases as the Dirac fermions relax. In contrast, normal massive carriers have positive photoconductivity and also decrease with decreasing carrier concentration. The photoinduced conductivity is showing a transmittance change caused by the optical pump, consistent with Figure 3a.

CONCLUSION

In conclusion, we have used optical-pump terahertz probe spectroscopy to characterize TCI $Pb_{1-x}Sn_xSe$ heterostructures. At low temperatures where the topological transition happens, one observes a negative photoinduced conductivity immediately after the photoexcitation, a result of the generation of hot surface state Dirac fermions. The relaxation of these Dirac fermions is relatively fast, occurring in about 6 ps. At room temperature, only normal massive carriers are observed, and the transmittance behaves like a normal photoexcited semiconductor, with a carrier lifetime of about 27 ps. At moderate temperatures, both carriers are observed. Our observations provide critical details for potential applications of Pb_{1-x}Sn_xSe and provide a direct measurement of the topological character of Pb_{1-x}Sn_xSe thin films, which will be of use for the characterization of more sophisticated bandstructure-engineered heterostructures.

AUTHOR INFORMATION

Corresponding Author

Zhenyang Xiao — Department of Electrical Engineering, University of Notre Dame, Notre Dame, Indiana 46556, United States; oorcid.org/0000-0002-3271-0803; Email: zxiao3@nd.edu

Authors

Jiashu Wang — Department of Physics, University of Notre Dame, Notre Dame, Indiana 46556, United States Xinyu Liu — Department of Physics, University of Notre Dame, Notre Dame, Indiana 46556, United States; ⊚ orcid.org/ 0000-0002-7004-6878

Badih A. Assaf — Department of Physics, University of Notre Dame, Notre Dame, Indiana 46556, United States;
ocid.org/0000-0002-6879-9651

David Burghoff – Department of Electrical Engineering, University of Notre Dame, Notre Dame, Indiana 46556, United States

Complete contact information is available at: https://pubs.acs.org/10.1021/acsphotonics.1c01717

Funding

All authors are funded by the NDnano Seed Grant Program. D.B. and Z.X. acknowledge support from the AFOSR under Grant No. FA9550-20-1-0192, from the NSF under ECCS-2046772, and from ONR under N00014-21-1-2735. B.A.A., J.W., and X.L. acknowledge support from NSF1905277 and DMR-1905277.

Notes

The authors declare no competing financial interest.

REFERENCES

- (1) Fu, L. Topological Crystalline Insulators. Phys. Rev. Lett. 2011, 106, 106802.
- (2) Zhang, X.; Wang, J.; Zhang, S.-C. Topological insulators for high-performance terahertz to infrared applications. *Phys. Rev. B* **2010**, 82, 245107.
- (3) Krizman, G.; Assaf, B.; Phuphachong, T.; Bauer, G.; Springholz, G.; Bastard, G.; Ferreira, R.; de Vaulchier, L.; Guldner, Y. Tunable Dirac interface states in topological superlattices. *Phys. Rev. B* **2018**, 98, 075303.
- (4) Hasan, M. Z.; Kane, C. L. Colloquium: topological insulators. *Rev. Mod. Phys.* **2010**, 82, 3045.

- (5) Qi, X.-L.; Zhang, S.-C. Topological insulators and superconductors. *Rev. Mod. Phys.* **2011**, *83*, 1057.
- (6) Hasan, M. Z.; Moore, J. E. Three-dimensional topological insulators. *Annu. Rev. Condens. Matter Phys.* **2011**, *2*, 55–78.
- (7) Woźny, M.; Szuszkiewicz, W.; Dyksik, M.; Motyka, M.; Szczerbakow, A.; Bardyszewski, W.; Story, T.; Cebulski, J. Electron-phonon coupling and a resonant-like optical observation of a band inversion in topological crystalline insulator $Pb_{1-x}Sn_xSe$. arXiv:2003.11849 [cond-mat.mtrl-sci] 2022, na.
- (8) Hsieh, T. H.; Lin, H.; Liu, J.; Duan, W.; Bansil, A.; Fu, L. Topological crystalline insulators in the SnTe material class. *Nat. Commun.* **2012**, *3*, 1–7.
- (9) Bosco, L.; Franckié, M.; Scalari, G.; Beck, M.; Wacker, A.; Faist, J. Thermoelectrically cooled THz quantum cascade laser operating up to 210 K. *Appl. Phys. Lett.* **2019**, *115*, 010601.
- (10) Kainz, M. A.; Semtsiv, M. P.; Tsianos, G.; Kurlov, S.; Masselink, W. T.; Schönhuber, S.; Detz, H.; Schrenk, W.; Unterrainer, K.; Strasser, G.; et al. Thermoelectric-cooled terahertz quantum cascade lasers. *Opt. Express* **2019**, *27*, 20688–20693.
- (11) Dhillon, S.; Vitiello, M.; Linfield, E.; Davies, A.; Hoffmann, M. C.; Booske, J.; Paoloni, C.; Gensch, M.; Weightman, P.; Williams, G.; et al. The 2017 terahertz science and technology roadmap. *J. Phys. D: Appl. Phys.* 2017, 50, 043001.
- (12) Palaferri, D.; Todorov, Y.; Gacemi, D.; Barbieri, S.; Li, L.; Davies, A.; Linfield, E.; Sirtori, C. Noise characterization of patch antenna THz photodetectors. *Appl. Phys. Lett.* **2018**, *113*, 161105.
- (13) Micheletti, P.; Faist, J.; Olariu, T.; Senica, U.; Beck, M.; Scalari, G. Regenerative terahertz quantum detectors. *APL Photonics* **2021**, *6*, 106102.
- (14) Hsieh, D.; Mahmood, F.; McIver, J.; Gardner, D.; Lee, Y.; Gedik, N. Selective probing of photoinduced charge and spin dynamics in the bulk and surface of a topological insulator. *Phys. Rev. Lett.* **2011**, *107*, 077401.
- (15) Kumar, N.; Ruzicka, B. A.; Butch, N.; Syers, P.; Kirshenbaum, K.; Paglione, J.; Zhao, H. Spatially resolved femtosecond pump-probe study of topological insulator Bi₂Se₃. *Phys. Rev. B* **2011**, *83*, 235306.
- (16) Sobota, J. A.; Yang, S.; Analytis, J. G.; Chen, Y.; Fisher, I. R.; Kirchmann, P. S.; Shen, Z.-X. Ultrafast optical excitation of a persistent surface-state population in the topological insulator Bi₂Se₃. *Phys. Rev. Lett.* **2012**, *108*, 117403.
- (17) Wang, Y.; Hsieh, D.; Sie, E.; Steinberg, H.; Gardner, D.; Lee, Y.; Jarillo-Herrero, P.; Gedik, N. Measurement of intrinsic Dirac fermion cooling on the surface of the topological insulator Bi₂Se₃ using time-resolved and angle-resolved photoemission spectroscopy. *Phys. Rev. Lett.* **2012**, *109*, 127401.
- (18) Hajlaoui, M.; Papalazarou, E.; Mauchain, J.; Jiang, Z.; Miotkowski, I.; Chen, Y.; Taleb-Ibrahimi, A.; Perfetti, L.; Marsi, M. Time resolved ultrafast ARPES for the study of topological insulators: The case of Bi₂Se₃. Eur. Phys. J.: Spec. Top. **2013**, 222, 1271–1275.
- (19) Christiansen, D.; Selig, M.; Malic, E.; Ernstorfer, R.; Knorr, A. Theory of exciton dynamics in time-resolved ARPES: Intra-and intervalley scattering in two-dimensional semiconductors. *Phys. Rev. B* **2019**, *100*, 205401.
- (20) Shi, S.-F.; Tang, T.-T.; Zeng, B.; Ju, L.; Zhou, Q.; Zettl, A.; Wang, F. Controlling Graphene Ultrafast Hot Carrier Response from Metal-like to Semiconductor-like by Electrostatic Gating. *Nano Lett.* **2014**, *14*, 1578–1582.
- (21) Hafez, H. A.; Chai, X.; Sekine, Y.; Takamura, M.; Oguri, K.; Al-Naib, I.; Dignam, M.; Hibino, H.; Ozaki, T. Effects of environmental conditions on the ultrafast carrier dynamics in graphene revealed by terahertz spectroscopy. *Phys. Rev. B* **2017**, *95*, 165428.
- (22) Jnawali, G.; Rao, Y.; Yan, H.; Heinz, T. F. Observation of a Transient Decrease in Terahertz Conductivity of Single-Layer Graphene Induced by Ultrafast Optical Excitation. *Nano Lett.* **2013**, 13, 524–530.
- (23) Lu, J.; Liu, H.; Sun, J. Negative terahertz photoconductivity in 2D layered materials. *Nanotechnology* **2017**, *28*, 464001.
- (24) Yang, X.; Luo, L.; Vaswani, C.; Zhao, X.; Yao, Y.; Cheng, D.; Liu, Z.; Kim, R. H. J.; Liu, X.; Dobrowolska-Furdyna, M.; Furdyna, J.

- K.; Perakis, I. E.; Wang, C.; Ho, K.; Wang, J. Light Control of Surface—Bulk Coupling by Terahertz Vibrational Coherence in a Topological Insulator. *npj Quantum Mater.* **2020**, *5*, 1–7.
- (25) Valdés Aguilar, R.; Qi, J.; Brahlek, M.; Bansal, N.; Azad, A.; Bowlan, J.; Oh, S.; Taylor, A. J.; Prasankumar, R. P.; Yarotski, D. A. Time-resolved terahertz dynamics in thin films of the topological insulator Bi₂Se₃. *Appl. Phys. Lett.* **2015**, *106*, 011901.
- (26) Sim, S.; Brahlek, M.; Koirala, N.; Cha, S.; Oh, S.; Choi, H. Ultrafast terahertz dynamics of hot Dirac-electron surface scattering in the topological insulator Bi₂Se₃. *Phys. Rev. B* **2014**, *89*, 165137.
- (27) Wang, J.; Liu, X.; Bunker, C.; Riney, L.; Qing, B.; Bac, S.; Zhukovskyi, M.; Orlova, T.; Rouvimov, S.; Dobrowolska, M.; et al. Weak antilocalization beyond the fully diffusive regime in Pb_{1-x}Sn_xSe topological quantum wells. *Phys. Rev. B* **2020**, *102*, 155307.
- (28) Krizman, G.; Assaf, B.; Phuphachong, T.; Bauer, G.; Springholz, G.; de Vaulchier, L.; Guldner, Y. Dirac parameters and topological phase diagram of Pb_{1-x}Sn_xSe from magnetospectroscopy. *Phys. Rev. B* **2018**, 98, 245202.
- (29) Bastard, G. Wave Mechanics Applied to Semiconductor Heterostructures; John Wiley and Sons Inc.: New York, NY, U.S.A., 1990
- (30) Novikova, N.; Yakovlev, V.; Kucherenko, I.; Vinogradov, V.; Aleschenko, Y. A.; Muratov, A.; Karczewski, G.; Chusnutdinow, S. Infrared Reflection Spectra of $Pb_{1-x}Sn_xSe$ (x=0.2,0.34) Topological Insulator Films on a ZnTe/GaAs Substrate and the Vibrational Modes of Multilayer Structures. *Semiconductors* **2018**, *52*, 34–40.
- (31) Kalish, S.; Chamon, C.; El-Batanouny, M.; Santos, L.; Sankar, R.; Chou, F. Contrasting the Surface Phonon Dispersion of Pb_{0.7}Sn_{0.3}Se in Its Topologically Trivial and Nontrivial Phases. *Phys. Rev. Lett.* **2019**, 122, 116101.
- (32) Tielrooij, K.; Song, J.; Jensen, S. A.; Centeno, A.; Pesquera, A.; Elorza, A. Z.; Bonn, M.; Levitov, L.; Koppens, F. Photoexcitation cascade and multiple hot-carrier generation in graphene. *Nat. Phys.* **2013**, *9*, 248–252.
- (33) Wu, L.; Brahlek, M.; Aguilar, R. V.; Stier, A.; Morris, C.; Lubashevsky, Y.; Bilbro, L.; Bansal, N.; Oh, S.; Armitage, N. A sudden collapse in the transport lifetime across the topological phase transition in $(\mathrm{Bi}_{1-x}\mathrm{In}_x)_2\mathrm{Se}_3$. Nat. Phys. **2013**, 9, 410–414.
- (34) Valdés Aguilar, R.; Wu, L.; Stier, A.; Bilbro, L.; Brahlek, M.; Bansal, N.; Oh, S.; Armitage, N. P. Aging and reduced bulk conductance in thin films of the topological insulator Bi₂Se₃. *J. Appl. Phys.* **2013**, *113*, 153702.